PNAS RESEARCH ARTICLE | BIOPHYSICS AND COMPUTATIONAL BIOLOGY

Cytoplasmic stirring by active carpets

Brato Chakrabarti[a,b,1], Manas Rachh[c], Stanislav Y. Shvartsman[a,d,e], and Michael J. Shelley[a,f,1]

Affiliations are included on p. 9.

Contributed by Michael J. Shelley; received March 13, 2024; accepted June 13, 2024; reviewed by Alexander N. Morozov and Stefano Di Talia

Large cells often rely on cytoplasmic flows for intracellular transport, maintaining homeostasis, and positioning cellular components. Understanding the mechanisms of these flows is essential for gaining insights into cell function, developmental processes, and evolutionary adaptability. Here, we focus on a class of self-organized cytoplasmic stirring mechanisms that result from fluid–structure interactions between cytoskeletal elements at the cell cortex. Drawing inspiration from streaming flows in late-stage fruit fly oocytes, we propose an analytically tractable active carpet theory. This model deciphers the origins and three-dimensional spatiotemporal organization of such flows. Through a combination of simulations and weakly nonlinear theory, we establish the pathway of the streaming flow to its global attractor: a cell-spanning vortical twister. Our study reveals the inherent symmetries of this emergent flow, its low-dimensional structure, and illustrates how complex fluid–structure interaction aligns with classical solutions in Stokes flow. This framework can be easily adapted to elucidate a broad spectrum of self-organized, cortex-driven intracellular flows.

cytoplasmic streaming | development | active matter | hydrodynamics | biophysics

Significance

In the egg cells of the fruit fly, *Drosophila melanogaster*, the emergence of cytoplasmic streaming presents a multiscale challenge that intersects developmental biology, transport phenomena, and nonequilibrium physics. The mechanics through which molecular machines orchestrate the robust intracellular streaming flow are highly complex. Here, we distill the key minimal ingredients driving this emergent dynamics by formulating a coarse-grained *active carpet* theory. Combining mathematical analysis, computations, and nonlinear theory, we reveal the topologies of these flows and illuminate how a complex, high-dimensional system always settles on a low-dimensional global attractor for swirling flows. Our findings unravel various universal aspects of fluid-mediated collective dynamics with potential implications for understanding cellular transport in other large cells.

Cells in the biome generally fall within the 2 to 30 μm range (1), primarily due to their dependence on inherently slow diffusion processes for intracellular transport. This suggests an evolutionary pressure to maintain the "right size" (2). However, exceptions exist. From egg cells and algal plant cells to slime molds and unicellular ciliates, cells can often reach several hundreds of microns or more in size. For these large cells, the transport and mixing of intracellular components by diffusion are extremely slow (3). Instead, they often manifest persistent, large-scale intracellular flows known as cytoplasmic streaming (4–8).

The stirring of cytoplasm is most commonly orchestrated by cytoskeletal elements at the cell cortex. This class of boundary-driven flows can be broadly divided into two categories. First, in which the active processes that generate these flows are predetermined during developmental stages. This results in a unidirectional coupling between cortical stresses and cytoplasmic flows. Notable examples of this process include the actomyosin-driven reorganizations seen in *Xenopus* egg extract (9–11), cytoplasmic streaming observed in algal cells (3, 12, 13), and the intracellular flows in amoeba spurred by cellular deformations (14). Here, we focus on the second category of cytoplasmic stirring that arises through the dynamical self-organization of the cytoskeletal elements driven by bidirectional feedback between bulk flows and cortical stresses. Two prominent examples of this are streaming flows in the oocytes of *Caenorhabditis elegans* (8) and the fruit fly, *Drosophila melanogaster* (15–19). In both of these examples, the flow is believed to emerge from fluid–structure interactions where nanometric molecular machines like Kinesin-1 traverse along flexible microtubules (MTs) anchored on the cell cortex, carrying payloads that entrain fluid (20–22). In the fruit fly, the interplay of entrained flow and collective deformation of anchored MT beds drives a self-organized vortical flow that spans the entire cell chamber of 100 to 300 μm (22).

To understand this self-organized flow in fruit flies, one study developed an active Brinkman-elastica model that describes the dynamics of an immersed and flexible MT bed upon which agents carry payloads (23). Special homogeneous solutions to this model, set in a 2D disk, showed that a global bending instability led to a large-scale vortex within the cavity. Recent large-scale computations of discrete motor-loaded MTs set in 3D geometries further elucidated the flow topologies (24). In the appropriate parameter regime, these simulations involving over a million degrees of freedom, consistently produce cell-spanning vortical flows, known as twisters, with remarkable robustness. Mathematically, this dynamics suggests that intracellular twisters are stable global attractors of a high-dimensional dynamical system. That said, how this complex fluid–structure interaction phenomenon converges to such a robust solution remains unknown. Here, we address this question by developing an *active carpet* model that is

Author contributions: B.C., S.Y.S., and M.J.S. designed research; B.C., S.Y.S., and M.J.S. performed research; M.R. contributed new computational tools; B.C. analyzed data; and B.C., S.Y.S., and M.J.S. wrote the paper.

Reviewers: A.N.M., The University of Edinburgh; and S.D.T., Duke University Hospital.

The authors declare no competing interest.

Copyright © 2024 the Author(s). Published by PNAS. This article is distributed under Creative Commons Attribution-NonCommercial-NoDerivatives License 4.0 (CC BY-NC-ND).

[1]To whom correspondence may be addressed. Email: brato.chakrabarti@icts.res.in or mshelley@flatironinstitute.org.

This article contains supporting information online at https://www.pnas.org/lookup/suppl/doi:10.1073/pnas.2405114121/-/DCSupplemental.

Published July 16, 2024.

Downloaded from https://www.pnas.org by 49.206.25.81 on April 28, 2025 from IP address 49.206.25.81.

analytically tractable and is suitable for embedding in 3D cellular geometries. Drawing inspiration from the intricate flows observed in the fruit fly, this model possesses the versatility to be tailored for elucidating a diverse range of cortically driven, self-organized cytoplasmic flows.

Active Carpet Theory

Our model approximates semiflexible MT filaments as rigid rods of length L anchored with their minus-ends to the cell cortex. At their anchoring point, these rods have a torsional spring that mimics the bending response of clamped, flexible filaments (8, 23, 25). We systematically perform this coarse-graining (Fig. 1) by calibrating the bending response of a flexible filament to rotations of an anchored rigid rod in a simple shear flow. This allows us to quantitatively map the torsional spring constant to the properties of the MT filament. Each rod acts as a track for the Kinesin-1 motor proteins, as illustrated in Fig. 1*B*. The forces from the plus-end directed cargos, propelled by these motor proteins, are coarse-grained into a uniform compressive force density, f_m. This force-density is directed along the bound MT toward its anchored minus end. Following Newton's third law, the motors exert an equal and opposite force on the cytoplasmic fluid. We characterize this dense MT carpet (17) by a uniform areal density c_0 and its orientation by a polarity field $\mathbf{n}(\mathbf{y}, t)$, where $\mathbf{y} \in \partial D$ is the surface coordinate on the cell boundary (Fig. 1). In this paper, we will denote any surface point by $\mathbf{y}$ and any point within the cytoplasmic volume by $\mathbf{x}$. The polarity field evolves according to Jeffery's equation (26) as

$$\partial_t \mathbf{n}(\mathbf{y}, t) = (\mathbf{I} - \mathbf{nn}) \cdot \nabla \mathbf{u}\Big|_{\partial D} \cdot \mathbf{n} + \frac{k_\varphi}{\xi_r} \mathbf{T}_0 \times \mathbf{n}. \qquad [1]$$

Here $\mathbf{u}(\mathbf{x}, t)$ is the emergent cytoplasmic fluid velocity that needs to be determined. The second term in Eq. **1** characterizes the response from the restoring torque on the rod. Here, $\xi_r = 4\pi\mu L^3/3\log(2/\varepsilon)$ with $\varepsilon \approx 10^{-3}$ being the aspect ratio of the rod and $\mu \sim 1$ Pa.s being the viscosity of the cytoplasm, which we model as an incompressible Newtonian fluid (18). The restoring torque $k_\varphi \mathbf{T}_0$ stems from the torsional spring of stiffness k_φ and penalizes deviation of the MT orientation from the inward unit surface normal $\hat{\boldsymbol{\vartheta}}(\mathbf{y})$. We estimate $k_\varphi \sim 4{-}5\, B/L$, where $B \approx 20$ pN.μm^2 (27) is the stiffness of a single MT fiber (Fig. 1*C*). The action of the molecular motors that drive the internal flow is approximated by a concentrated layer of stress jump $\bar{\mathbf{f}}(\mathbf{y}, t)$ across the interface ∂S delineated by the tips of the MT layer (Fig. 1*B*). Here we disregard the surface fluctuations of ∂S and define it as $\partial S := \partial D + L\hat{\boldsymbol{\vartheta}}(\mathbf{y})$. The quantitative impact of this simplification on the emergent dynamics is verified a posteriori. In the Stokesian limit of interest, the dimensionless governing equation for the momentum balance is then given as

$$-\nabla q + \Delta \mathbf{u} = \mathbf{0}, \quad \nabla \cdot \mathbf{u} = 0, \qquad [2]$$

$$\mathbf{u}(\mathbf{y}, t) = \mathbf{0}, \quad \text{on } \partial D, \qquad [3]$$

$$[\![\mathbf{u}]\!] = \mathbf{0}, \quad [\![\boldsymbol{\sigma} \cdot \hat{\boldsymbol{\vartheta}}]\!](\mathbf{y}, t) = -\bar{\mathbf{f}}(\mathbf{y}, t). \quad \text{on } \partial S. \qquad [4]$$

Here q is the fluid pressure, $[\![a]\!] = a|_{\partial S^+} - a|_{\partial S^-}$ denotes the jump of any variable across the interface ∂S, and $\boldsymbol{\sigma} = -q\mathbf{I} + (\nabla \mathbf{u} + \nabla \mathbf{u}^T)$ is the Newtonian stress tensor.

Using the MT length L as the characteristic length scale, the relaxation time $\tau_r \sim \xi_r/k_\varphi$ as the time scale and a viscous force scale, the parameters in the problem can be combined to yield two key dimensionless control parameters: i) $\bar{\rho} = c_0 L^2$ characterizing the surface density of the MT bed and ii) $\bar{\sigma} = \xi_r f_m/(\mu L k_\varphi)$ serving as a measure of activity. This dimensionless activity compares the relative strength of compressive motor forces to those derived from the restoring spring. There are two additional geometric parameters in the problem: i) $\mathcal{R} = L_s/L > 1$ is the ratio of the system size to the MT length and ii) $\chi = 2\pi/\log(2/\varepsilon)$ is a geometric constant that depends weakly on the aspect ratio ε of the MT. With this scaling, the dimensionless traction jump in Eq. **4** can be expressed as (*SI Appendix*)

$$\bar{\mathbf{f}}(\mathbf{y}, t) = \bar{\rho}\bar{\sigma}\mathbf{n} + \bar{\rho}\chi \left[\mathbf{T}_0 \times \mathbf{n} - \frac{\mathbf{n}\,\mathbf{n}\,\mathbf{n}}{2} : \nabla \mathbf{u}\Big|_{\partial D}\right]. \qquad [5]$$

The first term in Eq. **5** arises from the forces exerted by the Kinesin-1 motor proteins on the fluid (Fig. 1*B*). The second term represents forces stemming both from the torsional spring and from the rod's response in the mean-field fluid flow (*SI Appendix*). This completes our active carpet theory. In essence, our model integrates a boundary force field as defined by Eq. **5** to an internal homogeneous Stokes flow delineated in Eqs. **2**–**4**. The forcing and the emergent flow evolve self-consistently with a partial differential equation (PDE) that details the polarity of the MT bed as laid out in Eq. **1**. Here, we have ignored the possible variations of the MT density at the tips of filaments in the spirit of a long-wavelength theory. Furthermore, we highlight that in contrast with other problems of self-organized flows (28, 29), the dynamics of the polarity field does not involve any surface transport on the cell cortex. Its evolution is only coupled to

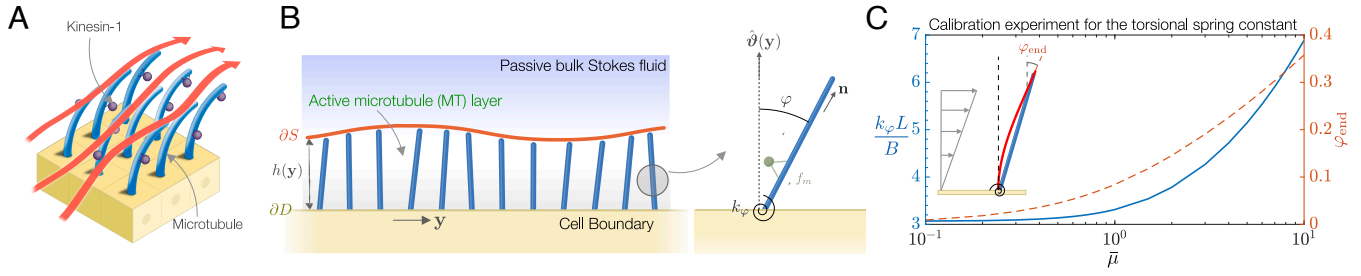

Fig. 1. Schematic of the experimental biological system, coarse-grained theory, and relevant approximations. (*A*) A magnified view on the cell boundary depicts the bent MTs in blue and molecular motors (kinesin-1) in purple, and the streaming flow in red. (*B*) A schematic illustrates the coarse-grained active carpet model of the streaming flow. MTs are approximated as rigid rods with a torsional spring at their anchoring point to the cell boundary. (*C*) We calibrate the spring stiffness k_φ using the deflection of a clamped MT fiber in a simple shear flow, approximated as a rigid rod of the same length L. The flow-strength is characterized by $\bar{\mu} = 8\pi\mu\dot{\gamma}L^4/(Bc)$, where μ is the fluid viscosity, $\dot{\gamma}$ is the shear rate, B is MT's bending rigidity, and $c = -\log(\varepsilon^2 \mathrm{e})$ is a geometric constant associated with the fiber aspect ratio ε. As $\bar{\mu}$ increases, so does the spring stiffness. We use the mean value over a range of $\bar{\mu}$ for which the filament deflections are moderate, resulting in $k_\varphi \approx 4{-}5\, B/L$.

Downloaded from https://www.pnas.org by 49.206.25.81 on April 28, 2025 from IP address 49.206.25.81.

the cytoplasmic flows through the velocity gradient on the cell boundary as seen in Eq. **1**.

Results

Streaming Flows in Half-Space. We initiate our exploration with simple, yet insightful dynamics within a 2D half-space. In this setup, an infinite planar array of fibers is anchored to a no-slip wall located at $z = 0$ (Fig. 2*A*). A fixed point for the system occurs when all the fibers are aligned along the z direction. In this configuration, represented as $\mathbf{n}_0 = \hat{\mathbf{z}}$, the motor-induced pushing forces renormalize the mean-field pressure, yielding $\mathbf{u}_0 = \mathbf{0}$. A small homogeneous transverse perturbation in the polarity field of the form $\mathbf{n} = \hat{\mathbf{z}} + \epsilon\varphi\hat{\mathbf{x}}$ ($\epsilon \ll 1$) evolves as,

$$\partial_t \varphi = [\bar{\rho}\bar{\sigma} - (\bar{\rho}\chi + 1)]\,\varphi. \qquad [6]$$

Here φ is the angle made by the rods with the $\hat{\mathbf{z}}$ axis. The first term in Eq. **6** is destabilizing and arises from an unidirectional shear flow in the active MT layer that tries to rotate the rods away from their upright position. The stabilizing second term is due to the restoring torque from the torsional spring. As evident from Eq. **6**, the fixed point becomes unstable when,

$$\bar{\sigma} > \left[\frac{1}{\bar{\rho}} + \chi\right]. \qquad [7]$$

This stability boundary, beyond which we observe steady streaming states, is shown in red in Fig. 2*A*. A plane-wave perturbation of the form $\epsilon\varphi(x) \sim \epsilon\hat{\varphi}_k e^{ikx+\lambda t}$, elucidates the wavenumber dependence of the growth rate as

$$\lambda(k) = -1 + \bar{\rho}e^{-k}(1-k)(\bar{\sigma} - \chi). \qquad [8]$$

The above dispersion relation accentuates the long-wavelength nature of the instability. We find that the homogeneous state, characterized by $k = 0$ is the most unstable wavenumber. This mirrors behaviors observed in instabilities of active suspensions (30). Further, from Eq. **8**, we observe that large wavenumbers experience exponential damping, and the growth rate asymptotes to $\lambda(k \to \infty) \to -1$ (Fig. 2*B*). This is in contrast to active-gel theories (31), where nematic elasticity results in an algebraic decay of the growth rate at high wavenumbers.

Nonlinear simulations further confirm that the emergent streaming state is homogeneous, characterized by a constant deflection angle φ_s of the MT bed with the $\hat{\mathbf{z}}$ axis. Fig. 2*C* illustrates this steady-state deflection angle for a given activity $\bar{\sigma}$, plotted against the MT bed density. We find, $\varphi_s \sim \sqrt{\bar{\rho} - \rho_c}$, close to the critical density ρ_c, indicating the hallmarks of a supercritical pitchfork bifurcation. In this emergent steady state, the fluid flow is constant and unidirectional above the MT layer and is characterized by the streaming speed u_s. At a given activity, the streaming speed increases with the bed density and is accompanied by increasing alignment of the MT fibers with the wall (Fig. 2*D*). Nonetheless, at large $\bar{\rho}$, hydrodynamic interactions between MTs become screened suggesting that the energy injected by the motor-proteins are dissipated at the scale of a single rod, resulting in a scaling of the form $\mu u_s^2 \sim f_m u_s$. This scaling law leads to a streaming speed independent of the MT density and increasing linearly with the motor force alone. Indeed, these observations are corroborated by the saturation of u_s with increasing density in Fig. 2*D* and its variation with the activity in Fig. 2*E*. Finally, our theory underscores the emergence of a fast relaxation time of the MT bed, arising from the collective hydrodynamic interactions. Analyzing the relaxational dynamics of an initially deflected bed (Fig. 2*E*) we determine this collective response time scale as $\tau_c \sim \tau_r/\bar{\rho}$, with $\tau_r \sim \xi_r/k_\varphi$ representing the single MT relaxation time. With these insights, we now ask, how this instability and the emergent flows are organized in an abstracted spherical egg cell, where topology prevents homogeneous solutions.

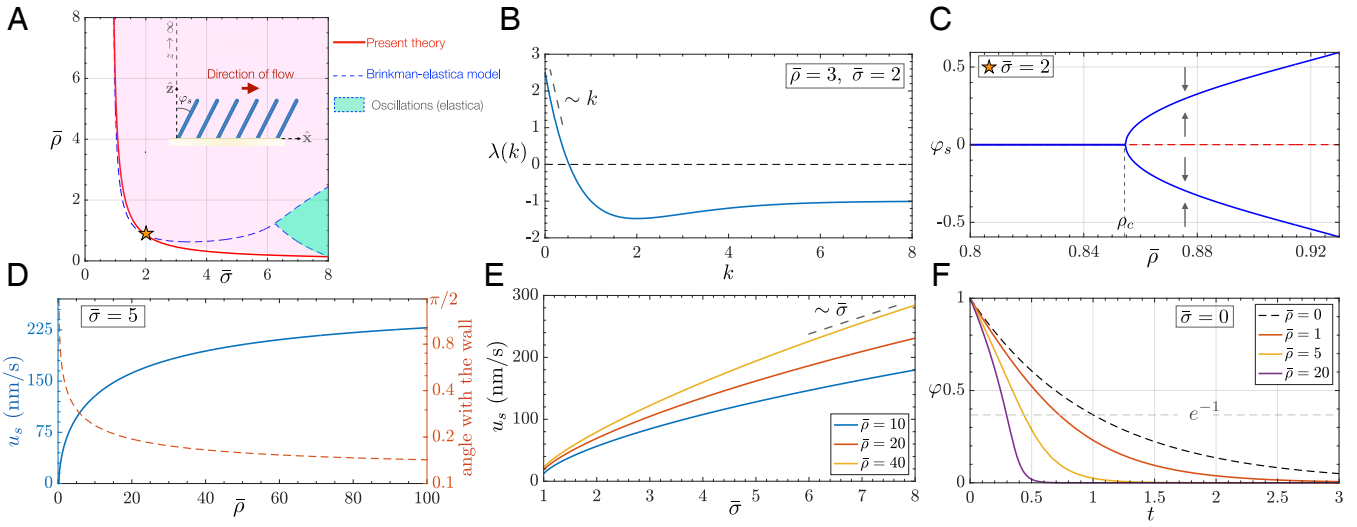

Fig. 2. Bifurcation analysis, streaming speeds, and relaxation dynamics in half-space. (*A*) Linear stability analysis (LSA) of the continuum theory predicts the emergence of a streaming state characterized by a homogeneous deflection of the MT bed (shown schematically). Overlaid on the stability boundary (depicted in red) are results from an active Brinkman-elastica model (in blue) obtained from ref. 23. Our active carpet model does not capture the oscillatory regime of the elastic filaments but agrees well for the prediction of streaming states. (*B*) Dependence of the growth rate λ on the plane wave number k. The growth rate is maximal for $k = 0$ indicating a long-wavelength instability and decreases linearly with k for small wavenumbers. Large-wavenumbers are exponentially damped and asymptotes to $\lambda = -1$. (*C*) Steady state deflection of the fiber bed as a function of $\bar{\rho}$. As evidenced by the bifurcation diagram, the streaming states arise from a supercritical pitchfork bifurcation of the straight MT bed. (*D*) Dimensional streaming speed u_s and the deflection of the MT bed relative to the wall as a function of $\bar{\rho}$. As $\bar{\rho} \to \infty$ the streaming speed asymptotes to a finite value. (*E*) At a given density $\bar{\rho}$, the streaming speed increases monotonically with activity. For large density, we find $u_s \sim \bar{\sigma}$. (*F*) Relaxation dynamics of a MT bed for various $\bar{\rho}$. The characteristic relaxation time of an isolated MT is $\tau_r \sim \xi_r/k_\varphi$. In the presence of hydrodynamic interactions, the bed relaxes faster, indicating the emergence of a collective relaxation time $\tau_c \sim \tau_r/\bar{\rho}$.

Downloaded from https://www.pnas.org by 49.206.25.81 on April 28, 2025 from IP address 49.206.25.81.

Integral formulation. To build toward our theoretical and computational investigation of 3D interior flows, we first highlight that solutions to Eqs. **2**–**4** can be written as (32, 33)

$$\mathbf{u}(\mathbf{x}) = \frac{1}{8\pi}\int_{\partial S} \bar{\mathbf{f}}(\mathbf{y})\cdot\mathcal{G}(\mathbf{x},\mathbf{y})\,\mathrm{d}\mathcal{A}(\mathbf{y}) - \frac{1}{8\pi}\int_{\partial D}\mathbf{f}^{w}(\mathbf{y})\cdot\mathcal{G}(\mathbf{x},\mathbf{y})\,\mathrm{d}\mathcal{A}(\mathbf{y}), \quad [9]$$

where $\mathcal{G}(\mathbf{x},\mathbf{y})$ is the free-space Green's function for the Stokes equation. In Eq. **9**, $\bar{\mathbf{f}}(\mathbf{y})$ is the traction jump across ∂S specified by Eq. **5** and $\mathbf{f}^{w}(\mathbf{y})$ is an unknown traction on the cell cortex ∂D. It is determined by imposing the no-slip condition $\mathbf{u}(\mathbf{y}) = \mathbf{0}$ on ∂D. This boundary-integral formulation allows fast simulations of flows inside smooth closed surfaces and helps us to derive analytical solutions for spherical egg cells as demonstrated below.

Emergent Vortex in a Sphere. We start by examining the emergence of streaming flows within a sphere of dimensionless radius $R > 1$. Analogous to the half-space analysis, a fixed-point of the system with $\mathbf{u} = \mathbf{0}$ arises when $\mathbf{n}_0 = -\hat{\mathbf{e}}_r$, where $\hat{\mathbf{e}}_r$ is the unit-outward normal to the sphere. To probe the stability of this state, we consider the evolution of a slightly perturbed polarity field $\mathbf{n} = -\hat{\mathbf{e}}_r + \epsilon\tilde{\mathbf{n}}(\theta,\phi)e^{\lambda t}$ $(\epsilon \ll 1)$, where $\tilde{\mathbf{n}}$ lies in the tangent-space of the sphere. Here, (r,θ,ϕ) represents the spherical coordinates, where $\theta \in [0,\pi]$ is the polar and $\phi \in [0,2\pi)$ is the azimuthal angle. Realizing that the associated flow $\mathbf{u} \sim \mathcal{O}(\epsilon)$, the evolution of the perturbation from the dimensionless form of the linearized Eq. **1** is given as

$$\lambda\tilde{\mathbf{n}} = -\partial_r\mathbf{u}\big|_{r=R} - \tilde{\mathbf{n}}. \quad [10]$$

As before, the first term in Eq. **10** is associated with a destabilizing shear-flow in the MT layer and the second term arises from the restoring torque. Drawing parallel to our plane-wave expansion in the half-space, we expand $\tilde{\mathbf{n}}$ on the basis of vector spherical harmonics (VSH) as

$$\tilde{\mathbf{n}}(\theta,\phi) = \sum_{\ell\geq 1,|m|\leq\ell} b_\ell^m\boldsymbol{\Psi}_\ell^m + c_\ell^m\boldsymbol{\Phi}_\ell^m. \quad [11]$$

Here we have introduced the set $\{\mathbf{Y}_\ell^m, \boldsymbol{\Psi}_\ell^m, \boldsymbol{\Phi}_\ell^m\}$, which are three orthogonal VSH of degree ℓ and order m (for $|m| \leq \ell$) with ℓ being the polar and m the azimuthal wavenumber (34) (*Materials and Methods*). Given a vector field represented in this basis, $\mathbf{Y}_\ell^m$ delineates its radial variation, $\boldsymbol{\Psi}_\ell^m$ accounts for the curl-free and $\boldsymbol{\Phi}_\ell^m$ the divergence-free component.

The Ansatz in Eq. **11** ensures that $\tilde{\mathbf{n}}$ is on the tangent space and the coefficients $\{b_\ell^m, c_\ell^m\}$ correspond to their specific amplitudes. We now recall that the integral operators defined by Eq. **9** diagonalize in the VSH basis (35–37). This observation motivates a solution approach in which we first expand the tractions in Eq. **9** on the chosen basis. On using the no-slip boundary condition we can then determine the unknown velocity $\mathbf{u}(\mathbf{x})$ in terms of $\tilde{\mathbf{n}}$. This allows us to obtain an analytical expression (*SI Appendix*) for the growth rate for each polar wavenumber ℓ as

$$\lambda(\ell) = -1 + \left(\frac{R-1}{R}\right)^{\ell+2}\bar{\rho}(\bar{\sigma}-\chi). \quad [12]$$

This expression is the central result from our linear theory and elucidates various facets of the instability. It predicts that the homogeneous fixed point becomes unstable for increasing activity or MT density and exhibits a weak dependency on the sphere size (Fig. 3*A*). Notably, as $R \to \infty$, we recover the stability threshold of the half-space, described by Eq. **7**. We further highlight that the dispersion relation is only a function of the quantized polar wavenumber ℓ and is independent of the azimuthal wavenumber m. This follows from the spectral properties of the integral operators as discussed in *SI Appendix*.

It is further evident from Eq. **7** that $\ell = 1$ emerges as the fastest growing mode and defines the stability boundary as seen in Fig. 3*A*. This mirrors the long-wavelength dynamics observed in the half-space as large polar wavenumbers are exponentially damped with $\lambda(\ell) \to -1$ as $\ell \to \infty$ (Fig. 3*B*). The dominant unstable eigenmodes are characterized by the divergence-free field $\boldsymbol{\Phi}_\ell^m$. Fig. 3 *C*-(i) shows the axisymmetric polarity field for the most unstable wavenumber $\ell = 1$. The associated fluid flow is reminiscent of a system-size *vortex*. As seen from Fig. 3 *C*-(i), this flow is characterized by a pure rigid-body rotation in the interior fluid and a shear flow in the MT layer, conforming to the no-slip boundary condition on the cell cortex.

Nonlinear Dynamics. Building on our understanding from the linear theory, we now probe the full nonlinear dynamics to explore the self-organization of emergent flows beyond the instability threshold. To this end, we start from a slightly perturbed base state and numerically evolve Eqs. **1**, **5**, and **9** simultaneously (*Materials and Methods*). Fig. 4*A* shows the evolution of the polarity field over time (portrayed on the exterior of the sphere). We characterize this evolution by color coding the surface by the local polar order parameter defined as

$$P(\theta,\phi) = \left\|(\mathbf{I}-\hat{\mathbf{e}}_r\hat{\mathbf{e}}_r)\cdot\mathbf{n}(\theta,\phi)\right\|. \quad [13]$$

As evident from Eq. **13**, regions of low polar order correspond to MTs being orthogonal to the cell surface. To further quantify the polarity field's spatiotemporal features, we seek a spectral expansion of the form $\mathbf{n}(\theta,\phi) = a_\ell^m\mathbf{Y}_\ell^m + b_\ell^m\boldsymbol{\Psi}_\ell^m + c_\ell^m\boldsymbol{\Phi}_\ell^m$. This approach allows us to introduce the power-spectrum, $\mathcal{P}_\ell(t)$ (*Materials and Methods*), which quantifies the azimuthally averaged energy content across all modes of a given polar wavenumber ℓ.

In Fig. 4*A*, we observe that starting from the nearly radial initial condition, the polarity field rapidly develops regions of high polar order over the collective response timescale, τ_c. These regions are indicative of well-aligned MT patches inducing flows parallel to their local orientations. This transient dynamics is confirmed by a marked reduction in the radial component associated with $\mathcal{P}_0$, accompanied by increased contributions from other wavenumbers in the power-spectrum, as shown in Fig. 4 *B*-(i). As the cytoplasmic flow ensues, it drives a self-organization across the system in which regions of high polar order compete and interact. These interactions progressively lead to the formation of pronounced low polar order patches and give birth to topological defects of charges both $+1$ (center) and -1 (saddles) as depicted in Fig. 4*A*. Always appearing in pairs, these disclination points in the surface polarity field preserve a global topological charge of two, satisfying the Poincaré-Hopf theorem. Ultimately, the system settles into a steady state, in which regions of high polar order coalesce, leaving us with an axisymmetric swirling state which we call a *twister* following ref. 24. As evident in the final snapshot, the alignment axis connects the two $+1$ defect centers on the two poles. The orientation and the chirality of the emergent field is determined by initial conditions. Fig. 4 *B*-(i) reveals that this final state is characterized by a dominant global contribution from $\ell = 1$ mode corresponding to a *vortex*

Downloaded from https://www.pnas.org by 49.206.25.81 on April 28, 2025 from IP address 49.206.25.81.

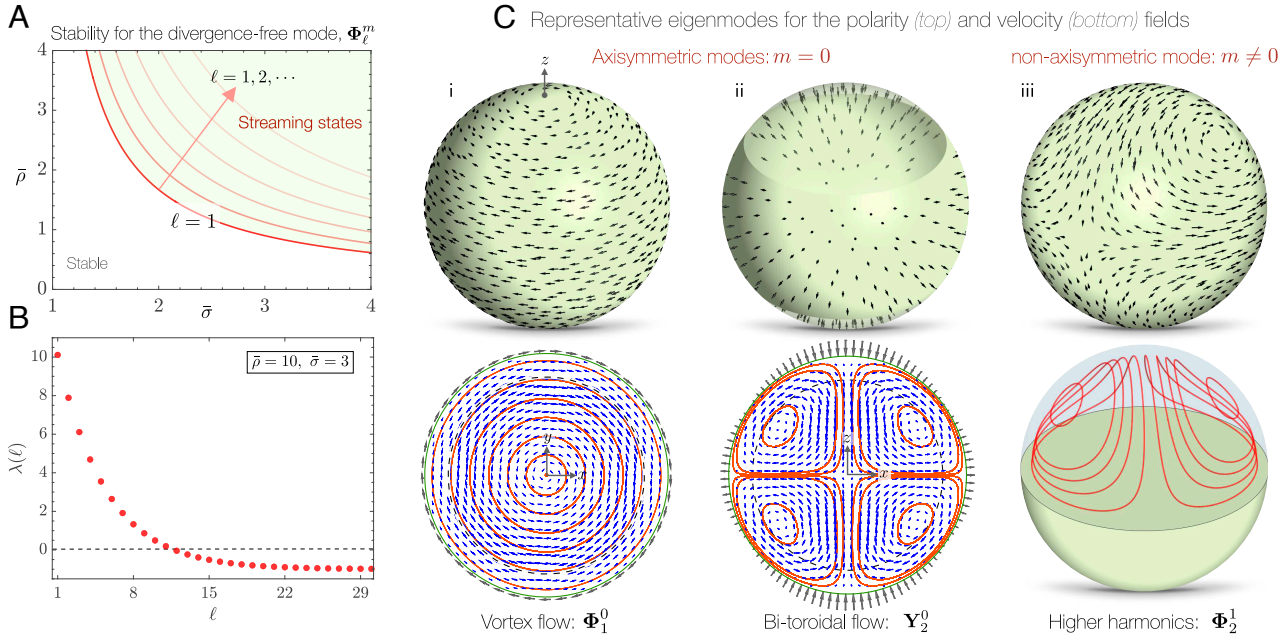

Fig. 3. LSA of streaming flows inside a spherical egg. (*A*) Stability boundary illustrating the onset of twisters within a sphere. The threshold for the instability is delineated by $\ell = 1$, representing the most unstable wavenumber. Successive curves in progressively lighter shades of red denote increasing discrete wavenumbers as they become unstable. (*B*) Variation of the growth rate $\lambda(\ell)$ with the polar wavenumber ℓ for a given MT density $\bar{\rho} = 10$ and activity $\bar{\sigma} = 3$. This highlights the long-wavelength nature of the instability. High wavenumbers are exponentially damped and asymptotes to -1 as $\ell \to \infty$. (*C*) Top row: Three representative surface polarity fields in terms of the VSH basis. The dominant unstable eigenmodes are characterized by $\mathbf{\Phi}_\ell^m$ and the subdominant one is given by $\mathbf{\Psi}_\ell^m$ (not shown). Bottom row: Corresponding interior flows with the dashed line in circular cross-section representing the surface ∂S. Axisymmetric modes with $m = 0$ exhibit a cell-spanning vortex (i) and a bitoroidal flow (ii). The nonaxisymmetric mode in (iii) illustrates saddles and a center in the polarity field. The associated flow-field is depicted for the upper hemisphere due to its mirror symmetry in the lower hemisphere. Here, we have fixed $R = 5$ corresponding to a dimensional radius of ~100 μm.

flow in the interior and weaker contributions from $\ell = 2, 3$. We further highlight in Fig. 4*C*, that the evolution toward this twister state is paired with a monotonic increase in the bending energy of the MT bed defined as

$$\mathcal{E} = \frac{1}{2} k_\varphi \int_{\partial D} \left[\cos^{-1}\left(-\hat{\mathbf{e}}_r \cdot \mathbf{n}(\theta, \phi)\right)\right]^2 \, \mathrm{d}A. \qquad [14]$$

This increase stems from the collective bending of the MTs induced by the emergent cytoplasmic flows. In the steady state, the energy injected by the molecular motors is balanced by the viscous dissipation in the cytoplasmic flows, which in turn maintain the bent conformation of the MT layer.

We now ask, how robust is this axisymmetric steady state? We test this by initiating the system with a different initial condition. The evolution of $\mathcal{P}_\ell(t)$ in Fig. 4 *B*-(ii) reveals that for this initial condition, the system quickly settles onto a low-dimensional manifold with a dominant contribution from the $\ell = 2$ mode. Our simulations indicate that this quasi-steady state closely aligns with the nonaxisymmetric eigenmode shown in Fig. 3 *C*-(iii). It stands distinct from the transient observed in the previous case, as seen in Fig. 4 *B*-(i). However, over a long time, the mode associated with the vortex flow ($\ell = 1$) grow, accompanied by the decrease of the $\ell = 2$ mode as before. The culmination is an analogous axisymmetric twister state, characterized by an identical power spectrum, which underscores the possibility of a single global attractor governing the collective dynamics.

Properties of the Twister Flow. The emergent axisymmetric, steady, streaming flow is strongly vortical. This emergent flow has excellent quantitative agreements with recent particle image velocimetry experiments on late-stage oocytes (24). Being driven by the local polarity field, the hydrodynamics interior to the MT layer resembles a rigid-body rotation spanning the entire cell size. In sync with our predictions from the linear theory, we find that the steady-state polarity field contains a dominant contribution from the $\mathbf{\Phi}_1^0$ [Fig. 3 *C*-(ii)] mode, responsible for the vortex flow. The flow in the plane of the vortex as shown in Fig. 5*B* is purely two-dimensional. In this plane, the fluid velocity increases almost linearly from the vortex core to the tips of the MT layer (Fig. 5*C*) followed by a sharp decrease in the active layer as it adapts to the no-slip boundary condition. However, this large-scale vortical flow now also features a secondary swirl component that channels fluid inward from the poles along the defect (or twister) axis (Fig. 5 *A* and *C*).

The structure of the weaker flow can be further elucidated by examining the spectral decomposition of the polarity field in its steady state. The spiraling pattern of this field around defects deviates from the pure vortex mode represented by $\mathbf{\Phi}_1^0$, leading to two key outcomes. First, a radial variation emerges in the orientation field, becoming pronounced near the defects where MTs point inward, conforming to the geometric constraint $|\mathbf{n}| = 1$. This behavior is represented by an axisymmetric mode $\mathbf{Y}_2^0$ shown in Fig. 3 *B*-(ii). Motor proteins push fluid along the MTs pointing inward near the poles, and incompressibility then induces a peripheral flow redirecting fluid back to the defect core. This pattern manifests as a pair of toroidal vortices around the defect axis, termed the bitoroidal flow, highlighted in Fig. 3 *B*-(ii).

The second component to this weaker flow stems from the deviation of the projected polarity field from the equatorial lines of the sphere. Appearing as a pair of sinks near the defects, this weak deviation is described by the curl-free axisymmetric mode

Downloaded from https://www.pnas.org by 49.206.25.81 on April 28, 2025 from IP address 49.206.25.81.

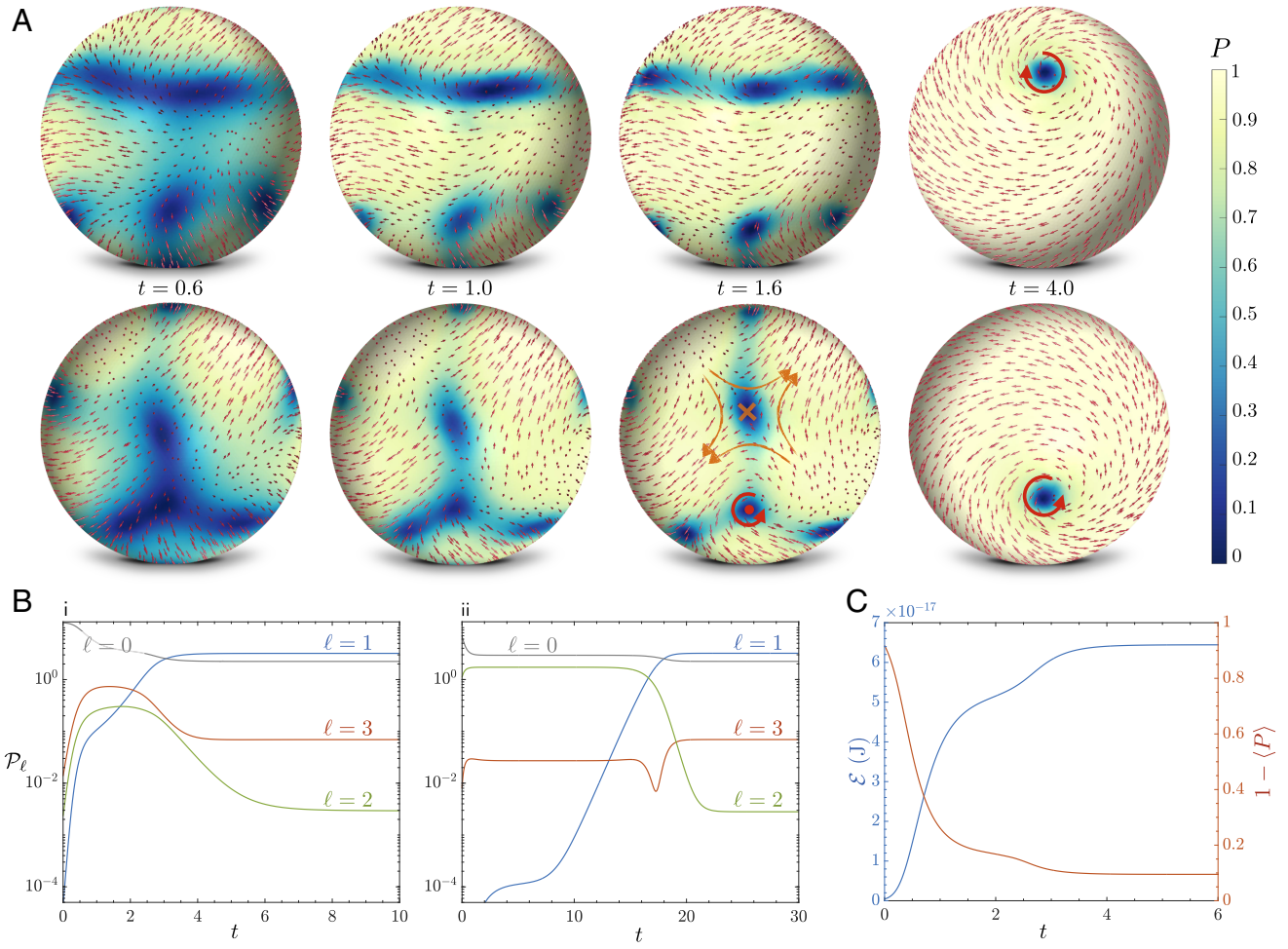

Fig. 4. Nonlinear dynamics and the pathway to the robust swirling state. (*A*) Multiple views of the snapshots from the evolution of the polarity field **n** are displayed by arrows on the exterior surface of the sphere. The surface is color coded by the local polar order parameter $P(\theta, \phi)$. Emergent topological defects with charge −1 (saddle) are marked by (×) and those with charge +1 (center) is marked by ∘. Time stamps are in terms of the dimensionless time scaled by the single MT relaxation time τ_r. (*B*) Evolution of the power spectrum of the polarity field under two different initial conditions. The base state of $\mathbf{n}_0 = -\hat{\mathbf{e}}_r$ corresponding to $\ell = 0$ was perturbed by i) including contributions from $\ell = 1, 2, 3$ and ii) from only $\ell = 2$ mode in the initial data. The mode $\ell = 1$ is associated with the emergent streaming flows. (*C*) The evolution of the dimensional elastic energy $\mathcal{E}$ alongside the average-polar order parameter $\langle P \rangle$. The increase in the bending energy is accompanied by a decrease in $1 - \langle P \rangle$ characterizing the aligned state of MTs. Parameters: $\bar{\rho} = 10$ (corresponding to roughly 3×10^3 MTs on the surface), $\bar{\sigma} = 3$, $\chi = 0.83$, and $R = 5$. The choice of $\bar{\sigma}$ corresponds to a dimensional motor force density of $f_m \sim 0.07$ pN/μm. Assuming a single motor force to be $\mathcal{O}(2$ pN) (38) leads to an estimate of 1 to 3 kinesin motors per MT (23).

$\mathbf{\Psi}_2^0$ (shown in *SI Appendix*). This arrangement of the polarity field incurs a tangential surface stress on the MT bed that induces a similar bitoroidal flow, reinforcing the previous contribution. We emphasize that the presence of this weaker flow in the emergent state is innately nonlinear, rooted in the topological necessity to have defects and the geometric constraints set by $|\mathbf{n}| = 1$.

Low-Dimensional Dynamics. Despite the complexity of our simulations and the excitation of several unstable wavenumbers (Fig. 3*A*), the streaming dynamics that surfaces is inherently low-dimensional. More importantly, its core characteristics can be distilled using select modes from the VSH basis. This insight prompts us to explore whether we can obtain coupled ordinary differential equations (ODEs) using a few salient modes that could encapsulate the essential features of this behavior. Accordingly, we propose an expansion for the polarity field as

$$\mathbf{n} = \underbrace{A(t)\mathbf{Y}_0}_{\text{radial}} + \underbrace{B(t)\mathbf{\Phi}_1^0}_{\text{vortex}} + \underbrace{C(t)\mathbf{Y}_2^0}_{\text{bitoroidal}} + \underbrace{D(t)\mathbf{\Phi}_2^1}_{m\neq 0}. \qquad [15]$$

Here, $\mathbf{Y}_0 = -\hat{\mathbf{e}}_r/\sqrt{4\pi}$ corresponds to the upright base state of the polarity field and $\{\mathbf{\Phi}_1^0, \mathbf{Y}_2^0, \mathbf{\Phi}_2^1\}$ respectively represent the modes associated with the vortex, bitoroidal, and nonaxisymmetric flows as illustrated in Fig. 3. We aim to derive the ODEs that govern the evolution of the time-dependent amplitudes $\{A(t), B(t) \cdots\}$ of each mode. The current form of the expansion is motivated by its simplicity and ease of physical interpretation. To obtain the amplitude equations, we first approximate the interfacial traction jump as $\bar{\mathbf{f}}(\mathbf{y}) \approx \bar{\rho}(\bar{\sigma} - \chi)\mathbf{n}$, a simplification reasonable near the bifurcation. We then use Eq. **9** in conjunction with the no-slip boundary condition to determine the velocity field $\mathbf{u}(\mathbf{x})$. Using this solution for the velocity field, we expand Eq. **1** up to fourth order in amplitude and use Galerkin projection to obtain the evolution equations (*SI Appendix*).

To illustrate this reduced dynamics, we initiate our analysis by considering the simplest case: a two-mode approximation. This encompasses the vortex mode and the homogeneous radial mode with $C = D = 0$. The ODEs governing the evolution of the two relevant modes are given as

Downloaded from https://www.pnas.org by 49.206.25.81 on April 28, 2025 from IP address 49.206.25.81.

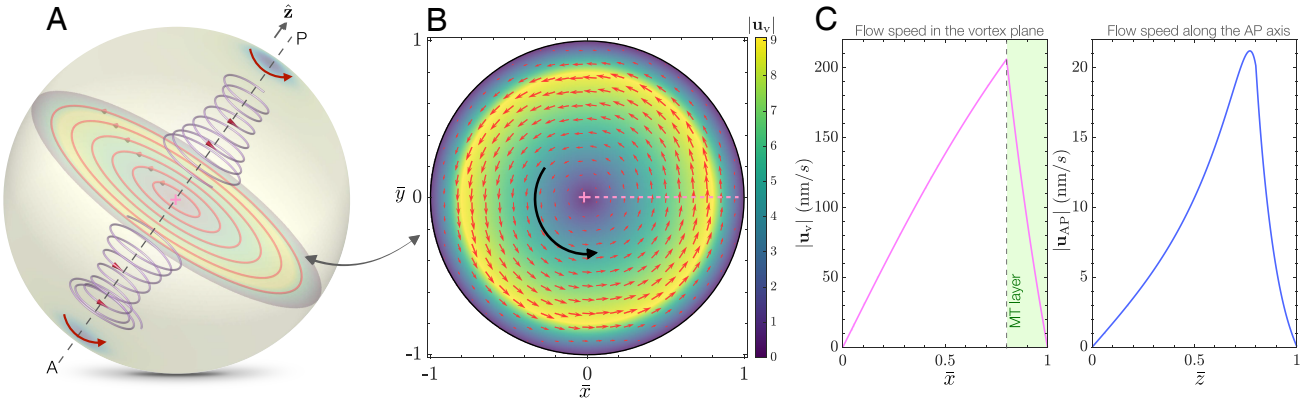

Fig. 5. Characteristics of the twister flow. (*A*) The vortex axis, joining the two +1 defects, is identified as the imaginary anterior–posterior (AP) axis of the abstracted cell. The vortex plane, together with the secondary swirling flow moving from the defect core to the center, is emphasized. (*B*) The flow interior to the MT layer in the plane of the vortex resembles rigid body rotation. The color code is for the dimensionless in-plane velocity. (*C*) Dimensional speed as a function of the normalized distance from the vortex center in the plane of the vortex (*Left*) and along the AP axis (*Right*). Parameters: same as in Fig. 4.

$$\frac{dA}{dt} = (A^2 - 4\pi)\mathcal{H}(A) - \mathsf{F}A^2B^2/4\pi^{3/2}, \quad [16]$$

$$\frac{dB}{dt} = AB\mathcal{Q}(A,B), \quad [17]$$

where $\mathsf{F} = \bar{\rho}(\bar{\sigma} - \chi)(R-1)^3/R^3$ and $\mathcal{H}(A)$, $\mathcal{Q}(A,B)$ are two quadratic polynomials (*Materials and Methods*). The base state $\mathbf{n} = -\hat{\mathbf{e}}_r$ is represented by $B = 0$ and $A = \sqrt{4\pi}$. As predicted by the LSA, this homogeneous radial state is unstable. The constraint of $|\mathbf{n}| = 1$ implies that the dynamics effectively exists along a single curve which is shown in Fig. 6*A*. The dynamics on this constrained manifold reveals that the system evolves toward a stable steady state marked by a nonzero amplitude of the vortex mode, inherently tied to a streaming flow. The emergence of two stable fixed points with contrasting signs for B signifies a lack of bias in the chirality of the vortex. This is further illustrated from the $B \to -B$ symmetry in Eqs. **16** and **17**. The associated interior flow-field has the structure shown in Fig. 3*C* consisting of a rigid-body rotation and a shear-flow in the MT layer.

Our next approximation is motivated by the existence of the weak bitoroidal flow in the full computations. To understand how nonlinear interactions spontaneously give rise to this secondary flow, we consider a three-mode approximation (*SI Appendix*, Eqs. **S70–S72**). This extends our previous case by including contribution from $\mathbf{Y}_2^0$ (the bitoroidal flow), while maintaining $D = 0$. As shown in Fig. 6*B*, starting from an initial condition of $C(0) = 0$, the reduced model evolves toward a steady streaming state with contributions from all three modes. Both the reduced model and computations reveal that this secondary flow consistently appears for any choice of parameters above the stability threshold. This persistence corroborates its truly nonlinear nature, embedded in the geometric constraints of the problem.

Our nonlinear simulations not only confirm the robust emergence of the axisymmetric twister in the steady state but also highlight transient nonaxisymmetric flows. This motivates us to understand the interactions between axisymmetric and nonaxisymmetric modes. To this end, we retain all the terms from Eq. **15** which now finally includes contribution from a nonaxisymmetric mode $\mathbf{\Phi}_2^1$ (*SI Appendix*, Eqs. **S73–S76**). The velocity field associated with this mode is shown in Fig. 3 *B*-(iii). To compare with our nonlinear simulations shown in Fig. 4 *B*-(ii), we choose initial conditions close to the base state and retain dominant contributions from this nonaxisymmetric mode. As revealed by Fig. 6*C*, the trajectory of amplitude evolution

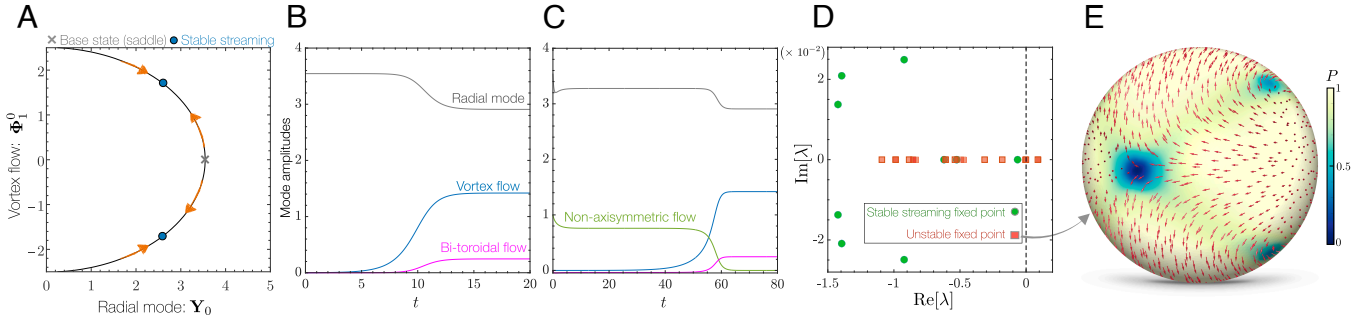

Fig. 6. Mode dynamics, the global attractor, and unstable exact solutions. (*A*) Phase space structure for a two-mode approximation to the streaming dynamics. The black curve represents the 1D manifold on which the dynamics is constrained to be in. (*B*) Amplitude evolution for a three-mode approximation. The bitoroidal flow spontaneously emerges through nonlinear mode interactions. (*C*) A four-mode approximation that now includes contribution from nonaxisymmetric mode dynamics. The initial saturation and eventual absence of the nonaxisymmetric mode hints at the possibility of unstable solutions in the problem. The emergent steady state corresponds to the stable fixed point obtained with the three-mode approximation. (*D*) Eigenspectra computed from a numerical LSA for the stable twister state (in green) and an exact unstable solution (in red); λ denotes the eigenvalues. This analysis highlights that the twister is an attractor of the dynamics. The unstable branch shown in (*E*) is computed numerically and features significant contributions from the nonaxisymmetric mode $\mathbf{\Phi}_2^1$ (Fig. 3) as hinted from the reduced model.

Downloaded from https://www.pnas.org by 49.206.25.81 on April 28, 2025 from IP address 49.206.25.81.

mirrors the power spectrum from the nonlinear simulations. In concert with the simulations, here we observe an initial amplitude saturation with nonaxisymmetric flows. However, nonlinear mode interactions cause the vortex mode to grow. Its growth is accompanied by the decay and eventual disappearance of the nonaxisymmetric component. This hints at the symmetries of the governing equations that allow the sustenance of only axisymmetric flows in steady states.

Discussion

The Journey toward a Global Attractor. Our simulations, combined with low-dimensional mode dynamics, firmly establish the robustness with which the cell transitions to the streaming state. To conclusively underscore that this is indeed a stable attractor, we numerically probed the stability of the emergent fixed point. The eigenspectra depicted in Fig. 6*D* provide evidence in support of this.

Fig. 4 revealed that starting from an almost straight configuration, the rapid onset of self-organization initiates over the fast timescale of τ_c. However, the duration for complete relaxation to the streaming state shows subtle dependence on the initial conditions. Further, the quasisteady transient dynamics [Fig. 4 *B*-(ii)] in simulations and in the reduced amplitude model, hint at the possibility of low-dimensional unstable attractors. Indeed, using a Newton–Krylov method on our governing PDEs, we numerically pinpointed one such unstable fixed point of the system, as illustrated in Fig. 6*E*. Strikingly, this unstable fixed point predominantly features the nonaxisymmetric, divergence-free $\mathbf{\Phi}_2^1$ mode, as previously alluded to by both simulations and the reduced dynamics. However, a cell is not perfect. It does not have uniformly distributed MTs, nor does it have a homogeneous activity of motor proteins. We speculate that this heterogeneity potentially makes the pathway toward the global attractor more robust enabling the formation of these streaming flows over a wide range of parameters. It remains to be seen how the stability of the global attractor is altered in the presence of intrinsic biochemical noise in the binding and force generation of the motor proteins.

Cells are also not spherical. In *Drosophila*, late-stage oocytes are best approximated as prolate ellipsoids with their aspect ratio being dynamic during the streaming phase as it grows in size (21). This broken symmetry in the problem raises the question: how the collective dynamics and the emergent flow topologies adapt to geometry. Recent computations seem to suggest that in these egg-shaped cells, flows tend to align with the AP axis (24) in contrast with the dynamics in a sphere, where symmetry precludes any preferential axis and the final orientation is purely set by initial conditions. How symmetry breaking leads to the loss of possible solutions and ultimately to the genesis of a single one remains unknown. Our coarse-grained PDEs provide an ideal framework to analyze such low-dimensional dynamics in future.

In summary, we have presented a coarse-grained active carpet theory for understanding cytoplasmic streaming inspired from the late-stage *Drosophila* oocytes. This theory has the form of a boundary force field coupled to an internal Stokesian flow and is the simplest mathematical abstraction within a hierarchy of models aimed at deciphering these intracellular dynamics (8, 23, 24). Through LSA, weakly nonlinear theory, and computations we have quantitatively recapitulated the key features of the emergent streaming flow. Here we provide insights into the low-dimensional organization of the collective dynamics and reveal the phase-space structure leading to the twister. We posit that our minimal description of the fluid–structure interaction holds the potential for adaptation across a spectrum of biological fluid mechanics problems: from transport in bacterial carpets to ciliated propulsion (39–42).

Materials and Methods

VSH. Here we provide the definition of the VSH used in the main text for analyzing solutions inside a sphere. Let $\theta \in [0, \pi]$ and $\phi \in [0, 2\pi)$ be the polar and azimuthal angles in the standard parameterization of the unit sphere. The scalar spherical harmonic Y_ℓ^m of degree ℓ and order m (for $|m| \leq \ell$) is defined in terms of the associated Legendre functions P_ℓ^m by

$$Y_\ell^m(\theta, \phi) = \sqrt{\frac{2\ell+1}{4\pi}}\sqrt{\frac{(\ell-|m|)!}{(\ell+|m|)!}}P_\ell^{|m|}(\cos\theta)e^{im\phi}. \quad [18]$$

The VSH $\{\mathbf{Y}_\ell^m, \mathbf{\Psi}_\ell^m, \mathbf{\Phi}_\ell^m\}$ of degree ℓ and order m (for $|m| \leq \ell$) are defined as (36)

$$\mathbf{Y}_\ell^m = -Y_\ell^m \hat{\mathbf{e}}_r, \quad [19]$$

$$\mathbf{\Psi}_\ell^m = \nabla_\gamma Y_\ell^m, \quad [20]$$

$$\mathbf{\Phi}_\ell^m = \hat{\mathbf{e}}_r \times \nabla_\gamma Y_\ell^m, \quad [21]$$

where $\nabla_\gamma = \partial_\theta \hat{\mathbf{e}}_\theta + \frac{1}{\sin\theta}\partial_\phi \hat{\mathbf{e}}_\phi$. Given a spectral representation of the polarity field $\mathbf{n}(\theta, \phi) = a_\ell^m \mathbf{Y}_\ell^m + b_\ell^m \mathbf{\Psi}_\ell^m + c_\ell^m \mathbf{\Phi}_\ell^m$ the power-spectrum is defined as

$$\mathcal{P}_\ell = \frac{1}{2\ell+1}\sum_m |a_\ell^m|^2 \langle \mathbf{Y}_\ell^m, \bar{\mathbf{Y}}_\ell^m \rangle + |b_\ell^m|^2 \langle \mathbf{\Phi}_\ell^m, \bar{\mathbf{\Phi}}_\ell^m \rangle + |c_\ell^m|^2 \langle \mathbf{\Psi}_\ell^m, \bar{\mathbf{\Psi}}_\ell^m \rangle. \quad [22]$$

Here we have introduced the inner-product of a vector $\mathbf{f}$ defined on the unit-sphere as

$$\langle \mathbf{f}, \bar{\mathbf{f}} \rangle = \int_0^{2\pi}\int_0^{\pi} \mathbf{f} \cdot \bar{\mathbf{f}} \sin\theta \, d\theta d\phi, \quad [23]$$

where $\bar{\mathbf{f}}$ denotes the complex conjugate.

2-Mode Synamics. Eqs. **16** and **17** provide the ODEs for the 2-mode approximation. The two polynomials appearing in these equations are given as

$$\mathcal{H}(A) = \frac{A}{\pi} - \frac{8\pi + A^2}{8\sqrt{\pi}}, \quad [24]$$

$$\mathcal{Q}(A, B) = \frac{40A\sqrt{\pi} - 5A^2\pi - 40\pi^2 + 16(5\pi - 3B^2)\mathrm{F}}{160\pi^{3/2}}, \quad [25]$$

where $\mathrm{F} = \bar{\rho}(\bar{\sigma} - \chi)(R-1)^3/R^3$.

Numerical Method. In order to solve for the emergent flows, we evolve Eqs. **1**, **5**, and **9** simultaneously. Given a polarity field $\mathbf{n}(\mathbf{y})$, Eq. **5** provides the traction jump across the fixed interface $\partial S := \partial D + L\hat{\mathbf{y}}$. We use a 5th-order accurate quadrature scheme to discretize the surface integrals of Eq. **9** and use quadrature by expansion to evaluate near interactions as outlined in refs. 43 and 44. For simulations presented here, we used $N \sim 2{,}700$ quadrature points on the spherical surface. Using the no-slip boundary condition provides us with an integral equation of the first kind for the unknown traction $\mathbf{f}^W$ on Eq. **9**. The resulting linear system for $\mathbf{f}^W$ is solved using GMRES that typically takes five to seven iterations. The velocity gradient on ∂D required for the evolution of the polarity field is then determined using a second-order accurate finite difference

Downloaded from https://www.pnas.org by 49.206.25.81 on April 28, 2025 from IP address 49.206.25.81.

approximation. The polarity field is evolved with a second-order accurate Runge–Kutta scheme with $\Delta t \sim 5{-}10 \times 10^{-3}$.

Data, Materials, and Software Availability. All study data are included in the article and/or *SI Appendix*. The computational tools for the simulations is freely available at https://github.com/fastalgorithms/fmm3dbie (45).

ACKNOWLEDGMENTS. We thank Jasmin Imran Alsous, Alexandra Jain, David Stein, Vicente Gomez Herera, David Saintillan, Dipanjan Ghosh, Sayantan Dutta, and Reza Farhadifar for illuminating discussions and helpful feedback. MJS acknowledges support by the NSF under Awards and DMR-2004469 and S.Y.S. acknowledges support from NIH grant no. R01GM134204.

Author affiliations: [a]Center for Computational Biology, Flatiron Institute, New York, NY 10010; [b]International Centre for Theoretical Sciences, Tata Institute of Fundamental Research, Bengaluru 560089, India; [c]Center for Computational Mathematics, Flatiron Institute, New York, NY 10010; [d]Department of Molecular Biology, Princeton University, Princeton, NJ 08544; [e]The Lewis-Sigler Institute for Integrative Genomics, Princeton University, Princeton, NJ 08544; and [f]The Courant Institute of Mathematical Sciences, New York University, New York, NY 10012

1. R. Milo, R. Phillips, *Cell Biology by the Numbers* (Garland Science, 2015).
2. J. B. S. Haldane, *On Being the Right Size* (Harper's Magazine, 1928).
3. J. Verchot-Lubicz, R. E. Goldstein, Cytoplasmic streaming enables the distribution of molecules and vesicles in large plant cells. *Protoplasma* **240**, 99–107 (2010).
4. J. W. van de Meent, I. Tuval, R. E. Goldstein, Nature's microfluidic transporter: Rotational cytoplasmic streaming at high Péclet numbers. *Phys. Rev. Lett.* **101**, 178102 (2008).
5. K. Yi *et al*., Dynamic maintenance of asymmetric meiotic spindle position through Arp2/3-complex-driven cytoplasmic streaming in mouse oocytes. *Nat. Cell Biol.* **13**, 1252–1258 (2011).
6. M. Almonacid *et al*., Active diffusion positions the nucleus in mouse oocytes. *Nat. Cell Biol.* **17**, 470–479 (2015).
7. S. N. Hird, J. G. White, Cortical and cytoplasmic flow polarity in early embryonic cells of *Caenorhabditis elegans*. *J. Cell Biol.* **121**, 1343–1355 (1993).
8. K. Kimura *et al*., Endoplasmic-reticulum-mediated microtubule alignment governs cytoplasmic streaming. *Nat. Cell Biol.* **19**, 399–406 (2017).
9. R. Sakamoto *et al*., Tug-of-war between actomyosin-driven antagonistic forces determines the positioning symmetry in cell-sized confinement. *Nat. Commun.* **11**, 3063 (2020).
10. N. Ierushalmi *et al*., Centering and symmetry breaking in confined contracting actomyosin networks. *eLife* **9**, e55368 (2020).
11. S. Shamipour, S. Caballero-Mancebo, C. P. Heisenberg, Cytoplasm's got moves. *Dev. Cell* **56**, 213–226 (2021).
12. B. Corti, *Osservazioni Microscopiche Sulla Tremella, e Sulla Circolazione del Fluido in una Pianta Acquajuola* (Rocchi, 1774).
13. F. G. Woodhouse, R. E. Goldstein, Cytoplasmic streaming in plant cells emerges naturally by microfilament self-organization. *Proc. Natl. Acad. Sci. U.S.A.* **110**, 14132–14137 (2013).
14. E. F. Koslover, C. K. Chan, J. A. Theriot, Cytoplasmic flow and mixing due to deformation of motile cells. *Biophys. J.* **113**, 2077–2087 (2017).
15. H. O. Gutzeit, R. Koppa, Time-lapse film analysis of cytoplasmic streaming during late oogenesis of Drosophila. *Development* **67**, 101–111 (1982).
16. J. B. Glotzer, R. Saffrich, M. Glotzer, A. Ephrussi, Cytoplasmic flows localize injected oskar RNA in Drosophila oocytes. *Curr. Biol.* **7**, 326–337 (1997).
17. M. E. Quinlan, Cytoplasmic streaming in the Drosophila oocyte. *Annu. Rev. Cell Dev. Biol.* **32**, 173–195 (2016).
18. S. Ganguly, L. S. Williams, I. M. Palacios, R. E. Goldstein, Cytoplasmic streaming in Drosophila oocytes varies with kinesin activity and correlates with the microtubule cytoskeleton architecture. *Proc. Natl. Acad. Sci. U.S.A.* **109**, 15109–15114 (2012).
19. P. Khuc Trong, H. Doerflinger, J. Dunkel, D. St Johnston, R. E. Goldstein, Cortical microtubule nucleation can organise the cytoskeleton of Drosophila oocytes to define the anteroposterior axis. *eLife* **4**, e06088 (2015).
20. W. Lu, V. I. Gelfand, Go with the flow-bulk transport by molecular motors. *J. Cell Sci.* **136**, jcs260300 (2023).
21. W. Lu, M. Winding, M. Lakonishok, J. Wildonger, V. I. Gelfand, Microtubule-microtubule sliding by kinesin-1 is essential for normal cytoplasmic streaming in Drosophila oocytes. *Proc. Natl. Acad. Sci. U.S.A.* **113**, E4995–E5004 (2016).
22. C. E. Monteith *et al*., A mechanism for cytoplasmic streaming: Kinesin-driven alignment of microtubules and fast fluid flows. *Biophys. J.* **110**, 2053–2065 (2016).
23. D. B. Stein, G. De Canio, E. Lauga, M. J. Shelley, R. E. Goldstein, Swirling instability of the microtubule cytoskeleton. *Phys. Rev. Lett.* **126**, 028103 (2021).
24. S. Dutta *et al*., Self-organized intracellular twisters. *Nat. Phys.* **20**, 666–674 (2024).
25. N. Pellicciotta *et al*., Cilia density and flow velocity affect alignment of motile cilia from brain cells. *J. Exp. Biol.* **223**, jeb229310 (2020).
26. L. G. Leal, *Advanced Transport Phenomena: Fluid Mechanics and Convective Transport Processes* (Cambridge University Press, 2007), vol. 7.
27. J. Howard, R. Clark, Mechanics of motor proteins and the cytoskeleton. *Appl. Mech. Rev.* **55**, B39 (2002).
28. F. C. Keber *et al*., Topology and dynamics of active nematic vesicles. *Science* **345**, 1135–1139 (2014).
29. S. Bell, S. Z. Lin, J. F. Rupprecht, J. Prost, Active nematic flows over curved surfaces. *Phys. Rev. Lett.* **129**, 118001 (2022).
30. D. Saintillan, M. J. Shelley, Active suspensions and their nonlinear models. *C. R. Phys.* **14**, 497–517 (2013).
31. F. Jülicher, S. W. Grill, G. Salbreux, Hydrodynamic theory of active matter. *Rep. Progr. Phys.* **81**, 076601 (2018).
32. C. Pozrikidis, *Boundary Integral and Singularity Methods for Linearized Viscous Flow* (Cambridge University Press, 1992).
33. J. Tanzosh, M. Manga, H. A. Stone, Boundary integral methods for viscous free-boundary problems: Deformation of single and multiple fluid–fluid interfaces. *Boundary Elem. Technol.* **VII**, 19–39 (1992).
34. E. Hill, The theory of vector spherical harmonics. *Am. J. Phys.* **22**, 211–214 (1954).
35. R. Schmitz, B. Felderhof, Creeping flow about a spherical particle. *Physica A* **113**, 90–102 (1982).
36. E. Corona, S. Veerapaneni, Boundary integral equation analysis for suspension of spheres in stokes flow. *J. Comput. Phys.* **362**, 327–345 (2018).
37. S. Kim, S. J. Karrila, *Microhydrodynamics: Principles and Selected Applications* (Courier Corporation, 2013).
38. K. Visscher, M. J. Schnitzer, S. M. Block, Single kinesin molecules studied with a molecular force clamp. *Nature* **400**, 184–189 (1999).
39. N. Darnton, L. Turner, K. Breuer, H. C. Berg, Moving fluid with bacterial carpets. *Biophys. J.* **86**, 1863–1870 (2004).
40. D. Lubkin, E. Gaffney, J. Blake, A viscoelastic traction layer model of muco-ciliary transport. *Bull. Math. Biol.* **69**, 289–327 (2007).
41. T. Ishikawa, T. Pedley, K. Drescher, R. E. Goldstein, Stability of dancing volvox. *J. Fluid Mech.* **903**, A11 (2020).
42. B. Chakrabarti, S. Fürthauer, M. J. Shelley, A multiscale biophysical model gives quantized metachronal waves in a lattice of beating cilia. *Proc. Natl. Acad. Sci. U.S.A.* **119**, e2113539119 (2022).
43. M. Rachh, A. Klöckner, M. O'Neil, Fast algorithms for quadrature by expansion. I: Globally valid expansions. *J. Comput. Phys.* **345**, 706–731 (2017).
44. E. Corona, L. Greengard, M. Rachh, S. Veerapaneni, An integral equation formulation for rigid bodies in stokes flow in three dimensions. *J. Comput. Phys.* **332**, 504–519 (2017).
45. T. Askham *et al*., fmm3dbie. GitHub. https://github.com/fastalgorithms/fmm3dbie. Accessed 1 January 2023.

Downloaded from https://www.pnas.org by 49.206.25.81 on April 28, 2025 from IP address 49.206.25.81.